Influence of solvent on the morphology and photocatalytic properties of ZnS decorated CeO2 nanoparticles

Cristiane W. Raubach, Lisânias Polastro, Mateus M. Ferrer, Andre Perrin, Christiane Perrin, Anderson R. Albuquerque, Prescila G. C. Buzolin, Julio R. Sambrano, Yuri B. V. de Santana, José A. Varela, and Elson Longo

Citation: Journal of Applied Physics **115**, 213514 (2014); doi: 10.1063/1.4880795
View online: http://dx.doi.org/10.1063/1.4880795
View Table of Contents: http://scitation.aip.org/content/aip/journal/jap/115/21?ver=pdfcov
Published by the AIP Publishing

Influence of solvent on the morphology and photocatalytic properties of ZnS decorated CeO_2 nanoparticles

Cristiane W. Raubach,[1,a)] Lisânias Polastro,[1] Mateus M. Ferrer,[1] Andre Perrin,[1,b)] Christiane Perrin,[1,b)] Anderson R. Albuquerque,[2] Prescila G. C. Buzolin,[2] Julio R. Sambrano,[2] Yuri B. V. de Santana,[3] José A. Varela,[3] and Elson Longo[3]
[1]*INCTMN-UFSCar, Universidade Federal de São Carlos, Rod.Washington Luís Km 235, São Carlos 13565-905, SP, Brazil*
[2]*Grupo de Modelagem e Simulação Molecular, INCTMN-UNESP, São Paulo State University, P.O. Box 47 3, Bauru 17033-360, SP, Brazil*
[3]*INCTMN-UNESP, Universidade Estadual Paulista, P.O. Box 355, Araraquara 14801-907, SP, Brazil*

(Received 9 November 2013; accepted 15 April 2014; published online 4 June 2014)

Herein, we report a theoretical and experimental study on the photocatalytic activity of CeO_2 ZnS, and ZnS decorated CeO_2 nanoparticles prepared by a microwave-assisted solvothermal method. Theoretical models were established to analyze electron transitions primarily at the interface between CeO_2 and ZnS. As observed, the particle morphology strongly influenced the photocatalytic degradation of organic dye Rhodamine B. A model was proposed to rationalize the photocatalytic behavior of the prepared decorated systems taking into account different extrinsic and intrinsic defect distributions, including order-disorder effects at interfacial and intra-facial regions, and vacancy concentration. © *2014 AIP Publishing LLC*.
[http://dx.doi.org/10.1063/1.4880795]

INTRODUCTION

The removal of organic pollutants from waste waters generated by the industry sector is an important challenge because these compounds are usually non-biodegradable. Unlike methods involving the transfer of organic pollutants to different phases, the advanced oxidation process (AOP)[1] which is a recently adopted approach affords complete destruction of the organic pollutants. In the AOP, a broad range of organic compounds are nonselectively oxidized by reactive species such as hydroxyl radicals.[2,3] Several approaches can be used to produce these active radicals, including the use of photocatalysts. Among the wide range of available photocatalysts, TiO_2 is the most widely used. Additionally, CeO_2 has been considered as a potential candidate, as detailed in previous reports.[4,5]

Many methods have been developed for the preparation of small particles, high surface area oxides, and mixed oxides suitable for catalytic applications. More specifically, several processing routes have been investigated to synthesize CeO_2 powders, including spray pyrolysis,[6] electrosynthesis,[7] gas condensation,[8] flux method,[9] sonochemical and microwave-assisted thermal decomposition,[10] hydrothermal method,[11] as well as precipitation from oxalate,[12] carbonate,[13,14] peroxide,[15] hydroxide,[16] and polymeric precursors,[17,18] including complexation with citric acid,[17] organometallic decomposition.[19] Previously, we reported the preparation of CeO_2 by a simple microwave-assisted hydrothermal (MAH) method.[20] We showed that the microstructure of the final cerium oxide crystals was very sensitive to the experimental conditions studied that included the cerium source, solvent, solution additives (such as surfactants), temperature, and reaction time. As recently reviewed, a wide variety of particle morphologies have been reported from spheres and cube to anisotropic polyhedra and rods.[20,21]

ZnS coverage of nanoparticles is well established method employed to enhance the specific physical properties of the base nanoparticles. An example of such a system is CdSe-ZnS core-shell particles prepared from zinc diethyldithiocarbamate $Zn(S_2CNEt_2)$ in an organic medium, such as tri-*n*-octylphosphine,[22] in the presence of oleylamine as a surfactant additive.[23] Earlier synthesis methods involved two different (and hazardous) precursors: diethyl zinc and bis(trimethylsilyl)sulfide,[24,25] zinc inorganic salts (chlorate and acetate) precipitated by sodium and ammonium sulfide,[26,27] have also been employed. Simpler inorganic precursors (metal oxide and elemental sulfur) have been proposed, however, these required high temperatures (230 °C) for dissolution.[28] In contrast, a low temperature (60 °C) synthesis can be achieved using zinc acetate and thiourea in 1-octadecene.[29] However, because of the low synthesis temperature, an additive is required to increase the solubility of the precursors at the low temperature.

In this paper, we report the synthesis of CeO_2, ZnS, and ZnS decorated CeO_2 nanoparticles using the microwave-assisted solvothermal (MAS) method that involves simple and nonhazardous chemicals as precursors and solvents, and affords the synthesis of different particle morphologies. The prepared particles were characterized X-ray diffraction (XRD), field-emission scanning electron microscopy (FE-SEM), energy-dispersive X-ray spectroscopy (EDS, elemental analysis), transmission electron microscopy (TEM), Fourier transform infrared (FT-IR) spectroscopy, ultraviolet-visible (UV-vis) spectroscopy, and photoluminescence (PL) spectroscopy. Subsequently, the photocatalytic activity of the

[a)]cristiane@liec.ufscar.br
[b)]On leave from Institut des Sciences Chimiques de Rennes, UMRCNRS 6226, Université de Rennes, 1, Rennes Cedex 35042, France.

synthesized particles was examined towards the photodegradation of organic dye Rhodamine B (RhB). The effect of particle morphology on the photocatalytic activity of the prepared particles is demonstrated.

EXPERIMENTAL DETAILS

Preparation of CeO_2 particles

First, 5×10^{-3} mol of $Ce(NO_3)_3.6H_2O$ (99% Vetec Química Fina) and 0.01 mol of cetyltrimethylammonium bromide (CTAB, 99.9% Acros Organics) were dissolved in 100 ml of a urea ($CO(NH_2)_2$) 0.5 M in either water or ethylene glycol (EG), under constant stirring at room temperature. The solution was transferred to a sealed Teflon autoclave (120 ml) and placed in a microwave oven (2.45 GHz, maximum power of 800 W). The reaction system was heated at 150 °C for 30 min at a heating rate of 10 °C/min. The pressure in the sealed autoclave was maintained at 3.3 atm. Following reaction, the autoclave was allowed to naturally cool to room temperature. The resulting white precipitate was collected, washed with water, and dried in air at room temperature. Then, the powder was calcined at 500 °C for 1 h, producing a straw yellow powder.

Preparation of ZnS decorated CeO_2 nanoparticles

The ZnS decorated CeO_2 nanoparticles were synthesized using 0.017 mol of the previously prepared CeO_2 powder dispersed in 25 ml of either water or EG (*solution 1*). Then, 0.017 (or 0.0017) mol of zinc chloride and 0.03 mol of thiourea were dissolved in 75 ml of either water or EG *(solution 2)* no surfactant was added at this stage. Solutions 1 and 2 were then mixed in a 120 ml Teflon autoclave and placed in the microwave system at 180 °C for 32 min. The resulting precipitates were washed several times with water until a neutral ($pH \approx 7$) solution was obtained, and the powders were collected and air dried at 100 °C for 5 h. For comparison, ZnS nanoparticles were also prepared from solution 2 under similar conditions. Table I list the various samples prepared in this study.

CHARACTERIZATION

Powder XRD data were collected in a 2θ range of 10°–105° using a step scanning mode of 0.02° step size and a 1 s/step, a 0.5° divergence slit, a 0.3 mm receiving slit, and Cu Kα1 radiation on a (Rigaku-DMax/2500PC). Microstructural characterization was performed on a field-emission scanning electron microscope Carl Zeiss Supra 35-VP and high-resolution transmission electron microscope FEI Tecnai G2TF20, operating at 200 kV. EDS (for elemental analysis) was conducted on the above mentioned scanning and transmission electron microscopes. FT-IR spectra were recorded in the range of 400–4000 cm^{-1} on a Bruker Equinox-55 (Germany) in transmittance mode using the KBr pellet technique. UV-vis spectra were collected on a Varian Cary 5G spectrophotometer in diffuse reflectance mode. PL spectra were collected using a Thermal Jarrel-Ash Monospec monochromator and a Hamamatsu R446 photomultiplier. Krypton ion laser (Coherent Innova) with an exciting wavelength of 350.7 nm (2.57 eV) was used, and the output of the laser was maintained at 200 mW. All measurements were taken at room temperature.

TABLE I. Concentrations of zinc ions, solvent used and identification of the samples synthesized by MAS method.

Sample	Identification	Solvent	Concentration (mol) zinc ion
CeO_2 pure	(CeO_2-EG)	EG	…
CeO_2@ZnS	(CZ1-EG)	EG	0.0017
CeO_2@ZnS	(CZ2-EG)	EG	0.017
CeO_2 pure	(CeO_2-H_2O)	H_2O	…
CeO_2@ZnS	(CZ1-H_2O)	H_2O	0.0017
CeO_2@ZnS	(CZ2-H_2O)	H_2O	0.017
ZnS pure	(ZnS-EG)	EG	0.017

PHOTOCATALYTIC ACTIVITY

The photocatalytic activity of the samples towards the photo oxidation of RhB dye [$C_{28}H_{31}ClN_2O_3$], (99.5%, Mallinckrodt) in aqueous solution was tested under UV-light illumination. First, 50 mg of catalyst powder was dispersed 50 ml of RhB solution (0.1 mM), adjusted to a pH of. The suspension was sonicated for 10 min in a Branson 1510 ultrasonic cleaner at a frequency of 42 kHz. Before illumination, the resulting suspension was stored in the dark for 10 min to allow equilibrium adsorption of RhB onto the catalyst. The solution containing beakers were then placed in the photo reactor at 20 °C and illuminated by six UV lamps (TUV Philips 15W) with maximum intensity at 254 nm. The light flux was measured by a Coherent Power Max PM10; the optical energy density was 20 mW cm^{-2}. At 30 min intervals, aliquots (2 ml) were sample and centrifuged at (9000 rpm) for 5 min to separate the powder from the solution. Changes in the absorbance at λ_{max} (520 nm) of the supernatant solutions were measured on a UV-vis dual beam spectrophotometer using a double monochromator and a photomultiplier tube detector (JASCO V-660). Reference photoactivity experiments containing different added radical scavengers (0.1 mmol) in the reaction system (ammonium oxalate as a scavenger for photogenerated holes,[30] $AgNO_3$ as a scavenger for photogenerated electrons,[31,32] *tert*-butyl alcohol as a scavenger for hydroxyl radicals,[30,33] and benzoquinone as a scavenger for superoxide radical species[34]) were performed under similar conditions to those employed for the above photocatalytic oxidation of samples.[35]

THEORETICAL METHODS AND MODELS

Periodic DFT calculations with the B3LYP hybrid function[36] were performed using a CRYSTAL09 computer code[37,38] that employ a Gaussian type basis set to represent Khon-Sham orbitals in periodic systems within the linear combination of atomic orbitals (LCAO) approximation. We have successfully used this method to study bulk and surfaces of oxides and sulfides.[39–42]

The CeO_2 fluorite structure (*Fm-3m*) is defined by one lattice parameter ($a = 5.41$ Å) (Ref. 43) where the cerium

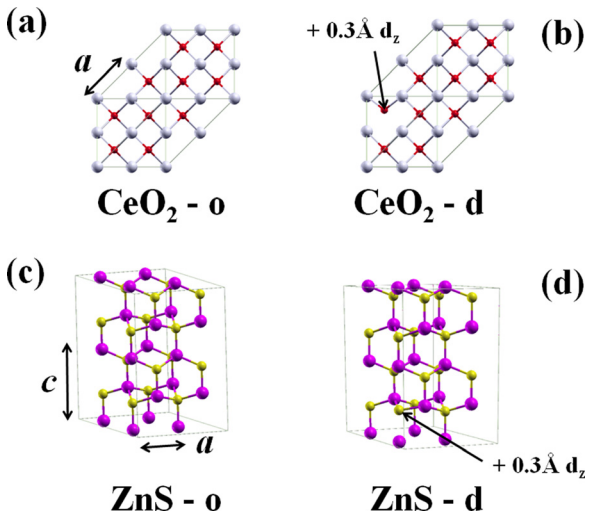

FIG. 1. Supercell $(2 \times 2 \times 2)$ from primitive unit cell of (a) CeO_2–o, (b) CeO_2–d, (c) ZnS–o, and (d) ZnS–d (labels o and d refer to ordered and disordered structures, respectively).

center is surrounded by eight oxygen atoms, which occupy tetrahedral sites [OCe_4] with a T_d local symmetry (see Fig. 1(a)). In contrast, the ZnS structure crystallizes either as rock salt (NaCl), cubic zinc blende, or hexagonal wurtzite structures.[44] Under normal conditions, the thermodynamically most stable phase is wurtzite. In the (*P63mc* structure), each Zn atom is surrounded by four S atoms [ZnS_4] at the corners of a tetrahedron (see Fig. 1(c)) with lattice parameters $a = 3.82$ Å and $c = 6.26$ Å.[44]

In CeO_2, oxygen centers are described by the all electron basis set 8-411d11G.[45] For cerium, a modified version of the small core ECP28MWB pseudopotential[46] (for core electrons) with valence shells was adopted as proposed by Désaunay *et al.*[47] within the contraction scheme: (16*s* 13*p* 10*d* 7*f*)/[4s 3p 3d 2f]. In the ZnS hexagonal crystal (*P63mc*), the atomic centers are described by the modified version[41] of the all electron basis set Zn_86-411d31G (Ref. 48) for Zn and S_86-311G for sulfur.[49]

The accuracy of the Coulombic and exchange integral calculations was controlled by five parameters were, set at (8 8 8 8 18). The shrinking (Monkhorst-Pack) factor was set at 6 which corresponds to 16k-points for CeO_2 and 34k-points for ZnS in the irreducible part of the Brillouin zone integration in primitive unit cells.

From the full optimized primitive cells, four periodic $(2 \times 2 \times 2)$ supercells were built to simulate the effects of a slight structural deformation on the electronic structure owing to the decorated architecture: (i) ordered structure CeO_2-o and ZnS-o (see Figs. 1(a) and 1(c)), and (ii) disordered structures CeO_2-d and ZnS-d (see Figs. 1(b) and 1(d)), where the O and S atoms are displaced by 0.3 Å in the [001 direction]. Fig. 1 shows ordered and disordered supercell models. These models are not intended to represent the exact reality of a disordered structure, but they offer a simple scheme to understand the concurrent effects in the resulting electronic structures.

Band structures were obtained for 100k-points along appropriate high-symmetry paths of the first Brillouin zone. The XCrySDen program[50] was used for the unit cell and density charge map designs.

RESULTS AND DISCUSSION

Structural identification

Fig. 2 illustrates the XRD patterns of CeO_2 and ZnS decorated CeO_2 nanoparticles synthesized at two different zinc solution concentrations prepared in either EG or water using the MAS method at 180 °C.

XRD patterns of CeO_2 prepared in either EG or water, and calcined at 500 °C were in full agreement with the data as obtained in the Inorganic Crystal Structure Database (ICSD) for this compound. Peak broadening, as assessed by the full width half maximum (FWHM) method, was observed when comparing samples synthesized in water with those prepared in EG.[51] This suggests that the particles prepared in EG were smaller. However, no significant changes in the patterns were apparent following decoration of the CeO_2 nanocrystals by ZnS. The blende phase is stable at low temperature. However, in the solution chemistry approach, both wurtzite[52] and blende[53–56] allotropes were formed. For comparison, a pure ZnS sample (prepared in EG) was synthesized under similar conditions and clearly appeared to be poorly crystallized wurtzite. However, because CeO_2 and blende ZnS are both face centered cubic structures with

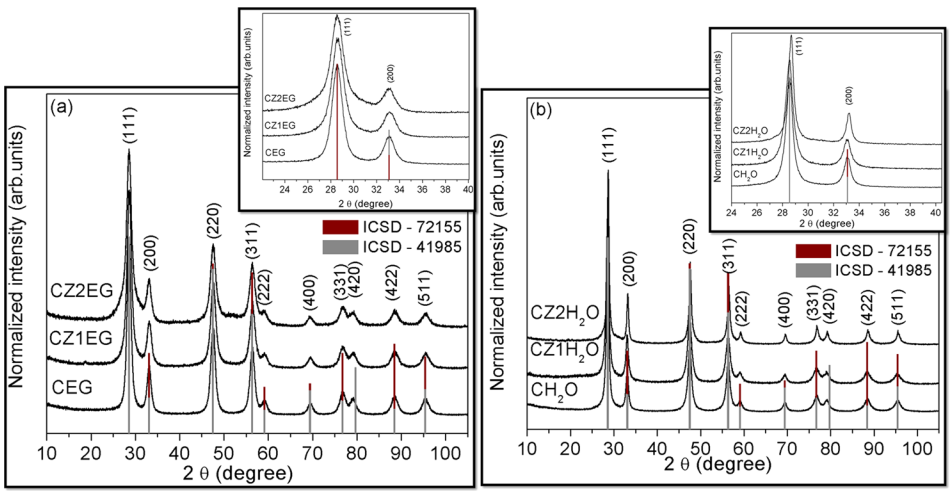

FIG. 2. XRD powder patterns of the CeO_2 and CeO_2/ZnS synthesized in (a) EG and (b) H_2O. Insets show the zoomed XRD patterns from 24° to 40°. The vertical lines indicate the position and relative intensity of the ICSD cards No. 72155 (CeO_2) and 41985 (ZnS blende).

comparable unit cell constants, we believe that the blende ZnS allotrope can be stabilized by epitaxial relationships. As a consequence, owing to the similarity of their patterns (illustrated by the bulk powder data reported in the ICSD files), it is not possible to experimentally prove the actual growth of a ZnS shell on the CeO_2 core solely from XRD data.

To overcome this limitation, EDS analyses were performed. As shown in Figs. 3(c) and 3(f), Zn and S peaks were observed in addition to Ce and O peaks. For layered samples of small dimensions, it is difficult to achieve an accurate quantitative analysis. However, the standard semi-quantitative results, obtained herein, were consistent with the expected Zn/S ratio (i.e., ~1).

A complete optimization procedure was adopted for determining lattice parameters *a* for CeO_2-o and *a, c*, and *u* for ZnS-o. The calculated and experimental values are shown in Table S2 and are in good agreement with results reported in the literature.[51]

The prepared particles were further examined by FT-IR spectroscopy.[51] The bands at 1610 and 3500 cm^{-1} confirmed that all samples, including CeO_2 particles, had water adsorbed on their surface (although the samples were previously fired at 500 °C (however, they were not stored under specific atmospheric moisture restrictions because they were subsequently used in a water environment). Owing to its fluorite structure, bulk CeO_2 displayed only one IR active Ce-O vibrational mode, slightly below 500 cm^{-1}. This band appeared at the lower limit of the detection range used in this study. However, several additional bands were clearly observed within the 700–1600 cm^{-1} range. These bands were ascribed to vibrational bond in molecules either coordinated or adsorbed on the surface. It should be noted that both CeO_2-EG and CeO_2-H_2O exhibited the same spectra, despite the different synthetic media employed. Because the samples were fired at 500 °C, the presence of urea and surfactant is improbable. Thus, these bands were probably associated with surface hydroxyls[20] and carboxyl groups (namely the bands near 1340 and 1540 cm^{-1}).[57–59] Comparison of CeO_2-EG and CZ1-EG samples confirmed that the extent of the splitting of the C-O vibration was lower in the latter samples. This is indicative, of a change from bidentate to monodentate coordination,[57] suggesting that at the very early stages of the ZnS growth, some of the Ce-O-C bonds were broken.

Conversely, most of the bands observed within the 500–1600 cm^{-1} range for pure ZnS particles (denoted as ZnS-EG in Fig. S1[51] agreed reasonably well with thiourea vibrations,[60] especially when comparing with $Zn[CS(NH_2)_2]_3^{2-}$ complexes.[61] Additionally, bands near 2915 and 3310 cm^{-1} that overlapped the hydroxyl broad absorption band were a close fit to bands corresponding to coordinated thiourea.[62] However, the most prominent feature

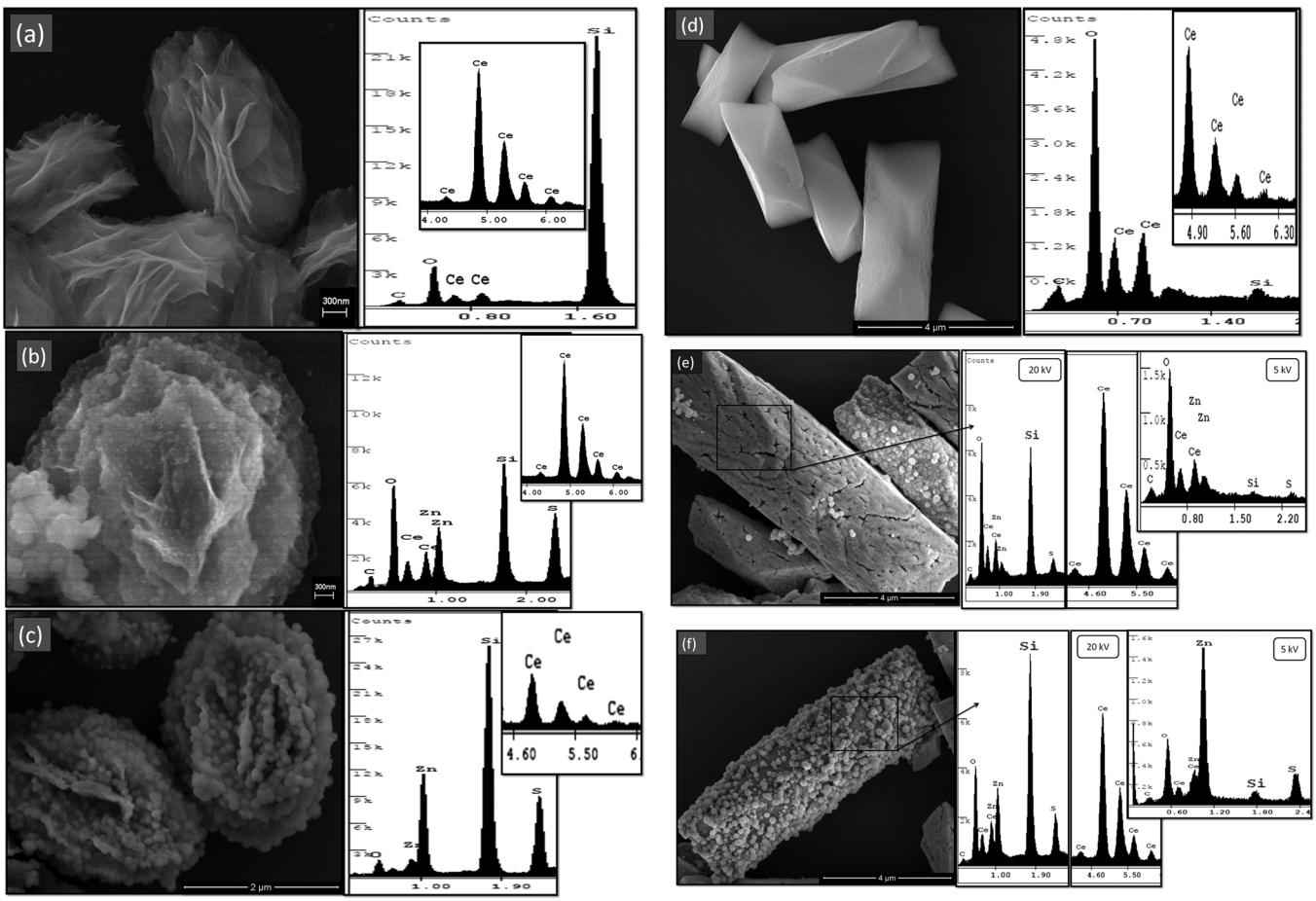

FIG. 3. FE-SEM images and EDS analysis of crystals synthesized by MAS method (a) CeO_2-EG, (b) CZ1-EG, (c) CZ2-EG, (d) CeO_2-H_2O, (e) CZ1-H_2O, and (f) CZ2-H_2O and EDS (20 kV and 5 kV) analysis.

TABLE II. Fermi level, top of valence band, bottom of conduction band, electronic band gap of ordered and disordered CeO_2 and ZnS by periodic B3LYP calculations and experimental values.

	Top of VB (eV)	Bottom of CB (eV)	Band gap (eV)	Experimental
CeO_2-o	−3.26 (O 2*p*)	−0.83 (Ce 4*f*)	2.43 (O 2*p* – Ce 4*f*)	…
		4.70 (Ce 5*d*)	7.96 (O 2*p* – Ce 5*d*)	
CeO_2-EG	…	…	…	3.10
CeO_2-H_2O	…	…	…	3.05
CeO_2-d	−3.17 (O 2*p*)	−0.83 (Ce 4*f*)	2.34 (O 2*p* – Ce4*f*)	…
		4.53 (Ce 5*d*)	7.70 (O 2*p* – Ce 5*d*)	
CZ1-EG	…	…	…	3.15
CZ2-EG	…	…	…	3.05
CZ1-H_2O	…	…	…	2.91
CZ2-H_2O	…	…	…	2.78
ZnS-o	−5.84 (S 3*p*)	−1.96 (Zn 3*d*)	3.88 (S 3*p* – Zn 3*d*)	4.20
ZnS-d	−5.82 (S 3*p*)	−1.97(Zn 3*d*)	3.85 (S 3*p* – Zn 3*d*)	

was the strong absorption band at ∼2140 cm^{-1}: the intensity of the band was stronger for the ZnS decorated CeO_2 and was maximum for the ZnS-EG particles. Thus, this band is clearly related to zinc sulfide; however, it is unlikely to correspond to Zn-O, Zn-S, and S-O vibrations owing to the strong intensity of the peak. In fact, only a few vibrators are possible in this spectral range, *e.g.*, S-H stretching vibration occurs at ∼2500–2600 cm^{-1} in H_2S and thiols.[63,64] Therefore, this vibration was tentatively assigned to weak S-H(OH) bond stretching present in species such as ZnS-H_2O that is consistent with the significant reduction in frequency observed. The other band at ∼1250 cm^{-1} that displayed similar behaviors would correspond to the same vibrator. The ZnS-EG spectrum data highlights an important point that bands characteristic of bound sulfur appear in the samples. In the case of the decorated compounds synthesized in water, a similar conclusion could not be made because of the unsuccessful preparation of pure ZnS-H_2O, possibly because of the compound hydrolysis in water.[51]

Microstructure analysis

Figs. 3(a)–3(f) show FE-SEM images of the samples synthesized by MAS method. The CeO_2 nanocrystals synthesized in water and EG exhibit different shapes and aspect ratios. A higher magnification analysis reveals that CeO_2-H_2O crystals are truncated parallelepipeds with flat surfaces, whereas the CeO_2-EG nanocrystals consist of open structures formed by sheets that tend to orientate parallel to each other, resulting in oval shaped particles. However, these sheets do not correspond to a specific orientation because no specific broadening (or narrowing) was observed in the XRD patterns, as confirmed by HR-TEM (see Fig. 4(c)). Different observations were made for the CeO_2 sample obtained by precipitation at room temperature in the presence of EG. A strong peak broadening was observed for the 111 peak while all other peaks remained narrow.[16] This was indicative of strongly anisotropic crystal growth with thin sheets developing parallel to the (111) plane.

Thus, simply changing the solvent (EG or water) enabled control over the shape of the resulting CeO_2 nanocrystals.

Mesoporous flower-like CeO_2 nanocrystals with an open structure were prepared by a hydrothermal method (simultaneous polymerization of a precipitation reaction, metamorphic reconstruction, and mineralization under hydrothermal conditions), followed by calcinations.[65,66] Unlike the CeO_2-EG samples prepared in this study that featured parallel sheets, those obtained nanospheres were composed of sheet-like crystallites oriented in flower petal-like fashions. Other flower-like CeO_2 architectures that consist of nanorods arranged in a spherical morphology, reminiscent of urchin structures, with no sheet-like components, have also been reported.[67]

Finally, when compared with the above CeO_2 samples, the MAS technique used herein for the synthesis of CeO_2 samples afforded a unique open structure when EG solution was used as solvent. In contrast, synthesis in water generated material morphologies as commonly reported.

After decoration of the CeO_2-H_2O and CeO_2-EG samples with ZnS, spherical particles were observed on both samples surfaces, indicative of the onset of ZnS nucleation during the coverage process. Some crystals in the CeO_2-H_2O samples were not covered, and resulting samples appeared quite porous. Under higher magnification analysis (see Fig. 3(e)), flat and elongated crystals were visible on the surface owing to the presence of a ZnS shell, as confirmed by EDS analyses. Comparison analysis with core-shell nanoparticles reported in the literature reveals that the shell is not uniformly developed around the core and the occurrence of nucleation of individual shell particles instead of the formation of a regular shell around the nanoparticles is common.[68,69]

Fig. 4 displays TEM images of the CeO_2-EG particles before and after zinc sulfide decoration. Fig. 4(a) confirms the microstructure of CeO_2-EG. Fig. 4(b) is a HR-TEM image of the thin sheet, as enlarged in Fig. 4(c). The images show that the cerium oxide nanocrystals (∼5–10 nm) are randomly oriented, as consistent with the relatively constant XRD FWHM values. Figs. 4(d) and 4(e) (in comparison with Fig. 4(b)) shows that ZnS (identified in the EDS analysis in Fig. 4(f)) grow onto the CeO_2 sheets as quasi spherical particles with a typical diameter of ∼50–60 nm.

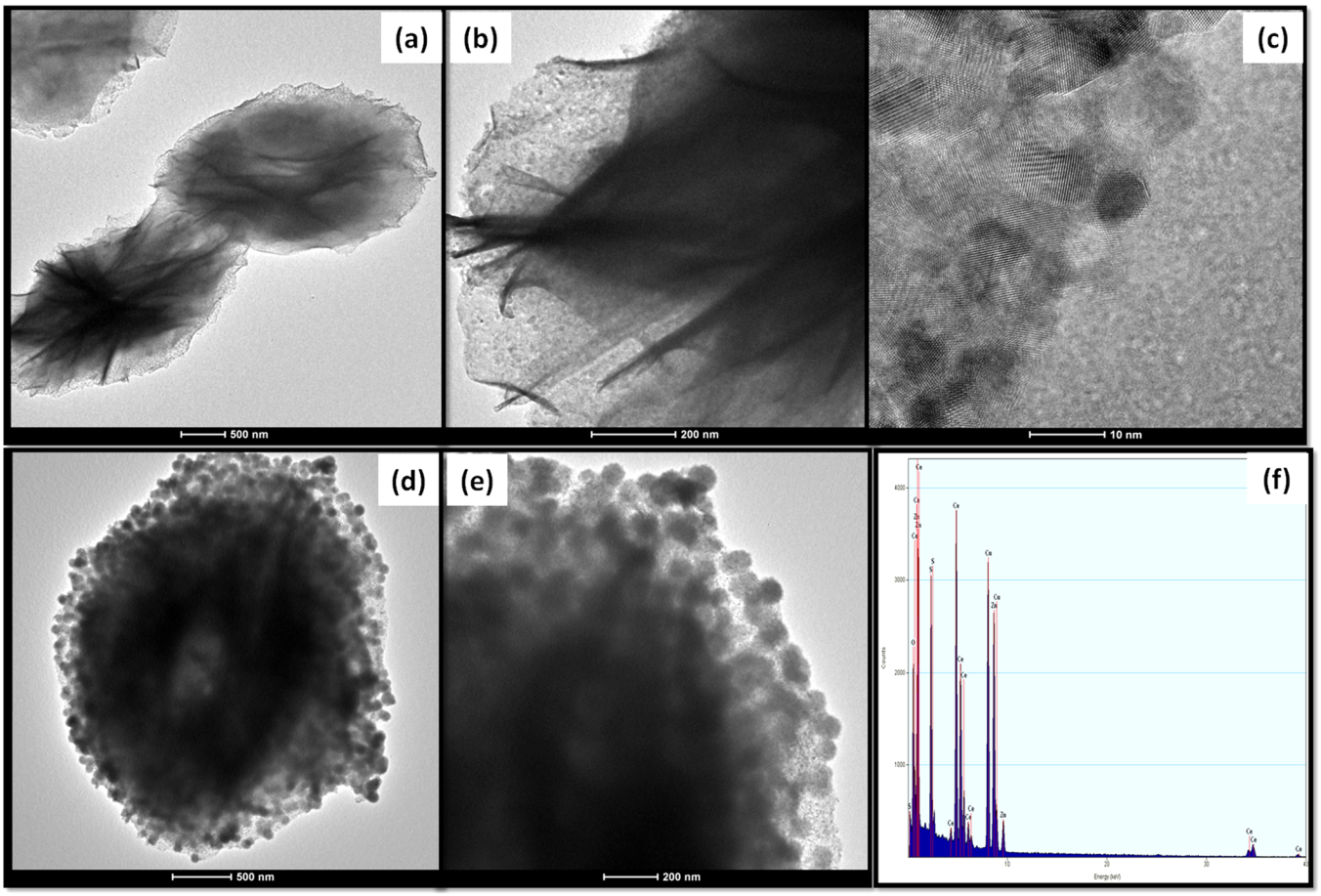

FIG. 4. The TEM images at different magnifications of the (a)-(c) CeO_2-EG and (d)-(e) CZ2-EG crystals; on the right: EDS analysis using 6 keV for energy, providing ratios Ce/O/Zn/S.

Absorption spectroscopy analysis

UV-vis spectral data of the samples are given in Table II; the band gap energies were calculated using the following equation: $(\alpha h\upsilon)^2 = f(h\upsilon)$.[70] Single crystal data confirm that ZnS exhibits a direct band gap of 3.66 eV for the blende allotrope and 3.74–3.78 eV for the wurtzite allotrope.[71] Additionally, a wurtzite band gap of (3.723 eV) was determined for wurtzite ZnS epilayers.[72] ZnS nanoparticles exhibited a blue shift that was related to a pronounced quantum confinement effect.[44,73] The band gap value (4.20 eV) for the wurtzite allotrope also indicated a blue shift. For CeO_2, the bulk optical band gap was reported as 3.14 eV, indicating the onset of non direct transitions in sputtered films.[74] Based on the optical studies of nanoparticles (2.6–4.1 nm), an indirect transition ($E_i = 2.87$ and 2.73 eV), and a direct transition ($E_d = 3.44$ and 3.38 eV) were observed. Despite the small increase in the band gap energy observed as the size decreased, no quantum size effects were evident in these nanoparticles.[75] *Inoue* reported optical band gaps of 2.90 and 3.52 eV for very small particles (2 nm), and concluded the presence of quantum size effects in these particles.[76] The optical band gaps of the prepared CeO_2 and ZnS decorated CeO_2 particles were within 2.78–3.10 eV. The decorated samples featured reduced band gaps (*i.e.*, red shift) that suggested the presence of interfacial interactions.

Importantly, the prepared CeO_2 and ZnS decorated CeO_2 samples featured absorption properties at the high energy region of the solar spectrum when compared with those of pure ZnS and TiO_2, thereby suggesting possible use under natural light.

For the disordered models, all lattice parameters remained constant because the small atomic dislocations and amount in bulk did not significantly modify these structural parameters. However, perturbation owing to anion shift induced symmetry breakage and splitting in the electronic band structure with a reduction in the band gap for the oxide and sulfide.[51]

Quantum mechanical calculations of the dislocated CeO_8 and ZnO_4 complex clusters indicated that localized states generated in the band gap reduced the gap energies (Table II). Levels above the valence band (VB) and below the conduction band (CB) of CeO_2-o are mainly composed of O-2*p* and Ce-5*d* orbitals, respectively, with unfilled Ce-4*f* orbital in the intermediate gap level.[51] Thus, two band gaps can be identified: 2.43 eV O-2*p* – Ce-4*f* (Γ-X) and 7.96 eV O-2*p* – Ce 5*d* (Γ-X) with a Fermi level of −3.26 eV. These results agree with theoretical results reported by *Sanz* and co-workers[77] who evaluated the use of hybrid functions to assess the properties of ceria oxide. Experimental studies have demonstrated that those two gaps in ceria are ∼−2.6–3.9 eV (O2p-Ce4f) and ∼6–8 eV (O2p-Ce5d).

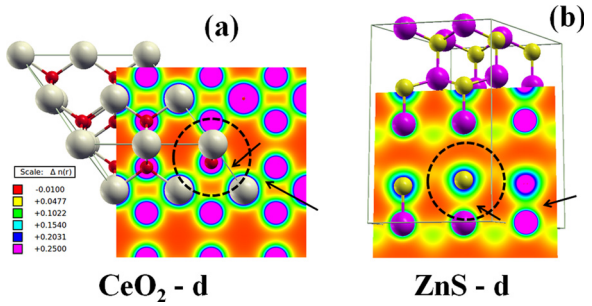

FIG. 5. Charge density maps of (a) CeO_2–d and (b) ZnS–d. The arrow inside the dotted circle region points the decrease of charge density due to the anion dislocation. The arrow outside the circle points the normal bond charge density between cation-anion.

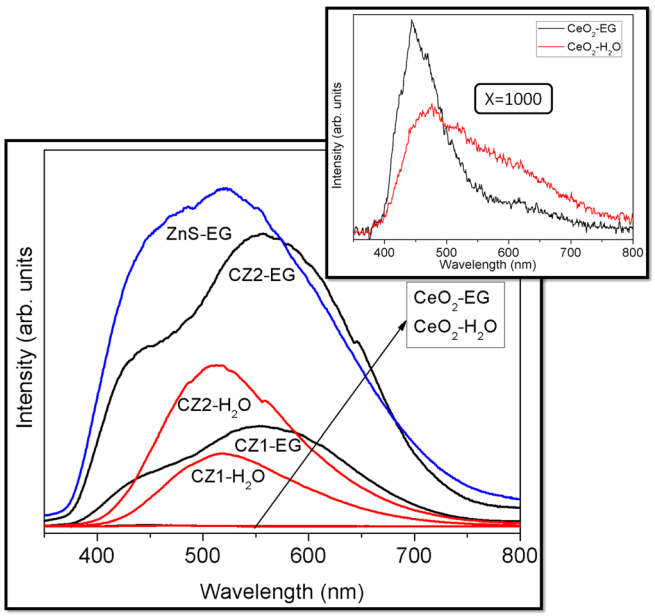

FIG. 6. Photoluminescence spectra of the CeO_2 and CeO_2/ZnS nanoparticles in EG and H_2O. Inset is a zoom of the PL spectra of CeO_2 in EG and H_2O where the intensities are enlarged by a factor 1000×.

For the CeO_2-d model, a decrease in the two band gaps values was observed that was mainly attributed to the split of the electronic levels.[51] However, a Fermi level increase was observed, owing to a cluster disorder, thereby clarifying that this disordered cluster was more reactive than the ordered cluster. The band gaps of CeO_2-d were 2.34 eV (O2p-Ce4f) (Γ-X), and 7.70 eV (O2p – Ce5d) (Γ-X).

The same band structure properties were observed for ZnS-o and ZnS-d. ZnS-o displayed direct band gap energy of 3.88 eV S-3p Zn 3d) with a Fermi level of −5.84 eV.[51] The ruptured local symmetry of the $[ZnS_4]^x$ cluster instigated splitting in the bands, a small increase (of∼0.02 eV) in the Fermi level, and a decrease in the gap to 3.85 eV.[77]

The $[CeO_8]$ and $[ZnS_4]$ cluster polarization, owing to a local disorder, can be visualized according to the charge density maps in Figs. 5(a) and 5(b), respectively. The defect is indicated by the region within the dotted circle showing a reduced cation-anion overlap region. Clusters outside the circle featured small electronic perturbation.

The present model though simple is useful to explain the disorder owing to the crystallite oxide sulfide interfaces in the core-shell representation. In this case, the band gap reductions were proportional to the short range disorder, and the increase in the Fermi level was related to the photoluminescence and photocatalytic effect of the polarized clusters, as discussed further.

Photoluminescence and photocatalytic activity

PL spectra confirmed the ZnS coverage of the CeO_2 decorated material. As observed in Fig. 6, the fluorescence emission of pure CeO_2 was not significant, where CZ1 and CZ2 exhibited PL spectra comparable that of ZnS-EG; the intensity increased with increasing Zn contents. The decorated samples prepared in water and EG displayed different fluorescence profiles. Similar behaviors have been reported in previous studies.[78,79] A detailed study on the mechanisms involved underway.

The photocatalytic activity of the samples towards the photodegradation of RhB is shown in Figs. 7(a) and 7(b). The two CeO_2 samples prepared in EG and water showed distinct photocatalytic activities. Nearly complete photodegradation of the dye solution was achieved over CeO_2-EG within 120 min, where only a small portion of the dye solution was degraded over CeO_2-H_2O within the same irradiation time. This behavior was obviously related to the different morphologies of the particles, thereby confirming that the photocatalytic properties of CeO_2 nanocrystals are strongly dependent on the shape of the particles.[80] As

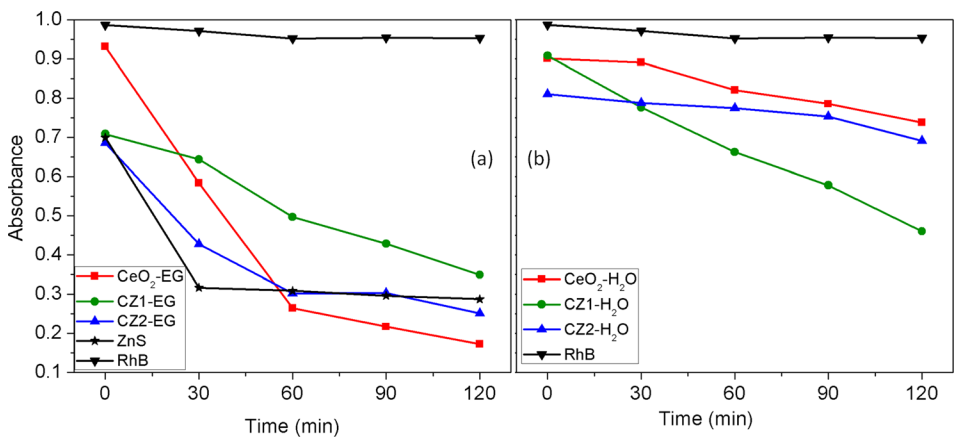

FIG. 7. Normalized absorbance of RhB solution after various times of under UV irradiation in presence of CeO_2, ZnS, and ZnS decorated CeO_2 synthesized in (a) EG and (b) H_2O.

exemplified further, lamellar CeO_2 crystals displayed an excellent photocatalytic yield towards the photodegradation of methylene blue.[4] The current mesoporous nanocrystals are of special interest because of their high surface to volume ratios and open structures that are suited for application in catalysis.

The ZnS-EG system shows intriguing photocatalytic results. Noticeable dye discoloration was observed prior to solution exposure to UV radiation. Under light exposure, degradation continues sharply before quickly reaching equilibrium. It is believed that the initial discoloration was related physical adsorption of the dye onto the surface, especially in the system involving ZnS.[81] However, this initial discoloration seldom occurred in the presence of the CeO_2-EG sample despite its very high surface area. Another possible explanation is that the as grown ZnS crystals possess activate sites that deactivate under illumination. Studies on the degradation and regeneration of ZnS catalysts[52] have shown strong changes following reaction cycles. In the latter regeneration study, the platelets that formed the microspherical structure of the catalyst disappeared following irradiation, yielding smooth ZnS spheres. Moreover, the resulting XRD pattern suggested the onset of severe amorphization. The initial characteristics of the ZnS catalyst were recovered by a new sulfidation treatment. In our system, we believe that ZnS could be oxidized by activated hydroxyls to produce $Zn(OH)_2$, xH_2O for instance.

The decorated sample exhibited different behaviors. For samples prepared in H_2O, a distinct improvement in the photocatalytic activity was observed for CZ1-H_2O relative to the (poorly efficient) CeO_2-H_2O sample. This could be ascribed to the decoration effect that promoted electronic transfer at the interface. However, when the thickness of the ZnS layer was increased, CZ2-H_2O started to behave like pure ZnS. For samples grown in EG, ZnS coverage reduced the porosity of the resulting decorated samples. Consequently, CZ1-EG displayed a low yield. Moreover, similar behaviors to those displayed by ZnS in the absence of light irradiation, as discussed earlier, were observed for CZ1-EG. Furthermore, when the ZnS layer thickness was increased, the CZ2-EG sample behaved as pure ZnS particles.

The cluster-like elucidation of the photocatalytic performance was supported and strengthened by different extrinsic (surface) and intrinsic (bulk) defect distributions including structural order-disorder effects (interfacial region, intra-facial region, and vacancy concentration). The application of stress or interfacial strain may induce significant modifications of the decorated sample band gap, thus promoting the development of a heterogenous structure. Thus, we consider that the bulk (CeO_2) and decorating (ZnS) components are neutral and have the same relevance in terms of the electronic structure. This effect only applies when there is an intermediate level of order-disorder between the interfaces of the decorated samples.

The defect structure and density variation in the interfacial and/or intra-facial regions may be responsible for the different photocatalytic properties of CeO_2, ZnS, and ZnS decorated CeO_2. Effective charge separation (electron/hole) requires the presence of a cluster to cluster charge transfer (CCCT) of electrons or holes from $[ZnS_4]_o^x$–$[ZnS_4]_d^x$, $[CeO_8]_o^x$–$[CeO_8]_d^x$, or $[CeO_8]_B^x$–$[ZnS_4]_S^x$ (decorated) (where o = order, d = disorder, B = bulk, and S = surface). A way to enhance the photocatalytic efficiency is to convert ordered complex clusters into disordered complex clusters. Consequently, the effect of surface properties on photocatalytic performance should be considered in terms of $[CeO_8]_o^x$, $[ZnS_4]_o^x$, or $[ZnS_4]_S^x$ clusters and $[CeO_8]_d^x$, $[ZnS_4]_d^x$, or $[CeO_8]_B^x$ clusters.

The first effect is intrinsic to CeO_2, ZnS, or ZnS decorated CeO_2 and is derived from the bulk/surface material composed of an asymmetric $[CeO_8]_d$ or $[ZnS_4]_d$ and ordered $[CeO_8]_o$ or $[ZnS_4]_o$. The ordered complex clusters often behave as electrons sinks, thereby improving charge separation within the semiconductor photocatalytic system. These electrons can then react with acceptors (O_2) at the interface, with a relatively lower overpotential of reduction. Consequently, the effect of surface properties on photocatalytic activity should be considered in terms of the following reactions:

$$[CeO_8]_o^x + [CeO_8]_d^x \xrightarrow{h\nu} [CeO_8]_o' + [CeO_8]_d^{\cdot}, \quad (1)$$

$$[ZnS_4]_o^x + [ZnS_4]_d^x \xrightarrow{h\nu} [ZnS_4]_o' + [ZnS_4]_d^{\cdot}, \quad (2)$$

$$[CeO_8]_B^x + [ZnS_4]_S^x \xrightarrow{h\nu} [CeO_8]_B' + [ZnS_4]_S^{\cdot}, \quad (3)$$

$$[CeO_8]_d^{\cdot} + H_2O \rightarrow [CeO_8]_d^x \ldots OH^* + H^{\cdot}, \quad (4)$$

$$[ZnS_4]_d^{\cdot} + H_2O \rightarrow [ZnS_4]_d^x \ldots OH^* + H^{\cdot}. \quad (5)$$

Upon absorption of a photon with energy equal to or greater than the band gap of the semiconductor, an electron/hole pair is generated in the bulk/surface. These charge carriers migrate towards the catalytic surface where charge transfer between the defect-free or defective surface and adsorbed oxygen molecules produces several types of charged species including O_2' superoxide ions. Molecular oxygen reactivity with $[CeO_8]$ or $[ZnS_4]$ results in further the species and subsequent oxygen incorporation into the lattice,

$$[CeO_8]_d^{\cdot} + O_2 + [CeO_8]_o' \rightarrow [CeO_8]_d^{\cdot} \ldots O_2'(ads) + [CeO_8]_o^x, \quad (6)$$

$$[ZnS_4]_d^{\cdot} + O_2 + [ZnS_4]_o' \rightarrow [ZnS_4]_d^{\cdot} \ldots O_2'(ads) + [ZnS_4]_o^x \quad (7)$$

$$[ZnS_4]_S^{\cdot} + O_2 + [CeO_8]_B' \rightarrow [ZnS_4]_S^{\cdot} \ldots O_2'(ads) + [CeO_8]_B^x. \quad (8)$$

The CeO_2, ZnS, ZnS decorated CeO_2 complex clusters react with water to produce hydroxyl radicals and hydrogen ions according to the following reactions:

The primary products formed from the partial oxidation reaction between water and complex cluster $[CeO_8]_d^{\cdot}$ or $[ZnS_4]_d^{\cdot}$ are hydroxyl radicals, OH*. These radicals exhibit high oxidation power that enables mineralization of organic compounds in water (anodic reaction). The primary reaction

(cathodic) involves the formation of superoxide species $[CeO_8]^{\cdot}_d \ldots O'_2$ or $[ZnS_4]^{\cdot}_d \ldots O'_2$. These species then react with hydrogen $H^{\cdot}$ to form a hydrogen peroxide radical (O_2H^*) according to the following reactions:

$$[CeO_8]^{\cdot}_d \cdots O'_2(ads) + H^{\cdot} \rightarrow [CeO_8]^{\cdot}_d \ldots O_2H^*, \quad (9)$$

$$[ZnS_4]^{\cdot}_d \cdots O'_2(ads) + H^{\cdot} \rightarrow [ZnS_4]^{\cdot}_d \ldots O_2H^*, \quad (10)$$

$$[ZnS_4]^{\cdot}_S \cdots O'_2(ads) + H^{\cdot} \rightarrow [ZnS_4]^{\cdot}_d \ldots O_2H^*. \quad (11)$$

The radicals OH^* and O_2H^* then react with the organic compound instigating the oxidation of the organic compound.

The nature of the superoxide and hydroxyl radicals can be described using a complex cluster model where the electron/hole transfers from the disordered structure to ordered structure, followed by absorption of molecular oxygen and water. The studies of the samples afforded the characterization of the defect-free and defective complex cluster structures and determination of surfaces with large numbers of defective complex clusters associated with morphological and structural properties. Fig. 8 illustrates electronic models of CeO_2 and ZnS ordered and disordered structure before and after O_2 and H_2O interaction.

Further, understand the nature of primary active species, semiconductor (Eqs. (1)–(3)) and degradation agent (Eqs. (4)–(11)), involved for visible light degradation of RhB in an aqueous phase over the CeO_2/ZnS nanoparticles, we have carried out the control experiments with adding scavenger for electrons for electrons (e′), holes ($h\cdot$), hydroxyl radicals (OH*), and superoxide radicals (O_2H^*). Fig. 8 shows the results of adding different radical scavengers over the CeO_2/ZnS photocatalyst reaction system under UV irradiation. When the radical scavenger, tert-butyl alcohol (TBA) for OH* and benzoquinone (BQ) for O_2H^*, are added into the reaction system, the degradation of RhB is significantly inhibited (Figs. 9(a) and 9(b)), these results suggests that, under UV irradiation, the OH* and O_2H^* (Eqs. (7)–(11)) play an important role toward the degradation of RhB over the CeO_2/ZnS nanoparticles.

Indeed, the addition of electron scavenger, $AgNO_3$ (Ag) and hole scavenger ammonium oxalate (AO) to the reaction

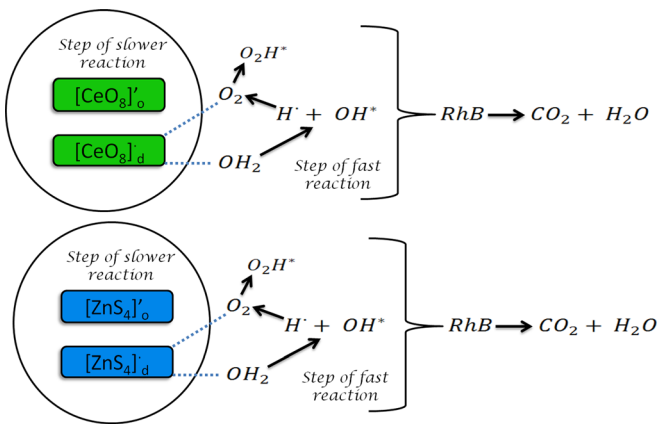

FIG. 8. Mechanism models of ZnS decorated CeO_2 system interface in the photodegradation process.

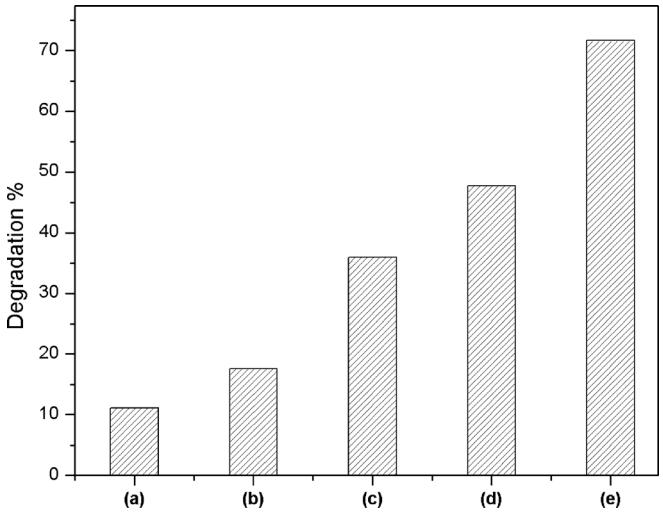

FIG. 9. Controlled experiments using different radical scavengers for the photocatalytic selective degradation of RhB over CeO_2/ZnS in an aqueous solvent; (a) reaction with tert-butyl alcohol (TBA), as a scavenger for hydroxyl radicals (OH*), (b) reaction with benzoquinone (BQ) as a scavenger for superoxide radicals (O_2H^*), (c) reaction with ammonium oxalate (AO) as a scavenger for photogenerated holes ($h\cdot$), (d) reaction with $AgNO_3$ as a scavenger for photogenerated electrons (e′), and (e) the reaction in the absence of radical scavengers under UV irradiation for 120 min.

system had intermediate effects on the photodegradation of RhB (Figs. 9(c) and 9(d)). Thus, OH* and O_2H^* radicals cannot be formed before polarization of the semiconductor and reaction with water and oxygen, Eqs. (1)–(8). The reaction over ZnS decorated CeO_2 is primarily driven by photogenerated electrons and holes in the semiconductor that subsequently, reacts with water, Eqs. (1)–(5).

CONCLUSIONS

CeO_2, ZnS, and ZnS decorated CeO_2 nanoparticles were synthesized by the efficient MAS method and their properties were investigated in detail. FE-SEM and TEM analyses confirmed a clear relationship between the nature of the solvent used in the synthesis and resulting CeO_2 crystals morphologies. Truncated parallelepipeds with flat surfaces were obtained using water as a solvent where oval particles with an open structure built from sheets were obtained using EG as a solvent. The presence of ZnS on the surface of CeO_2 was evidenced by EDS analyses and IR spectroscopy. The decorated nanoparticles exhibit characteristic absorption bands in the IR spectra that were also visible in the pure ZnS sample. More specifically band that was attributed to weak S-H bonding in Zn-S-H-OH surface species was observed. The intensities of the PL spectra were directly related to the amount of ZnS used in the synthesis. The photocatalytic studies of these nanoparticles support a clear relationship between the particle morphology and RhB degradation rate. Finally, a model was proposed to explain the photocatalytic behavior of these decorated systems taking into account different extrinsic and intrinsic defect distributions, including order-disorder effects at interfacial and intra-facial regions and vacancy concentration.

ACKNOWLEDGMENTS

The authors are thankful for the financial support of Brazilian research financing institutions: CAPES, CNPq, and FAPESP process Nos.: 2010/19484-0 and 2012/17500-3.

[1]W. H. Glaze, J. W. Kang, and D. H. Chapin, Ozone-Sci. Eng. **9**, 335 (1987).
[2]S. Das, P. V. Kamat, S. Padmaja, V. Au, and S. A. Madison, J. Chem. Soc.-Perkin Trans. **2**, 1219 (1999).
[3]Y. Q. Yang, D. T. Wyatt, and M. Bahorsky, Textile Chem. Colorist **30**, 27 (1998).
[4]F. J. Chen, Y. L. Cao, and D. Z. Jia, Appl. Surf. Sci. **257**, 9226 (2011).
[5]L. W. Qian, J. Zhu, W. M. Du, and X. F. Qian, Mater. Chem. Phys. **115**, 835 (2009).
[6]H. Wang, J. J. Zhu, J. M. Zhu, X. H. Liao, S. Xu, T. Ding, and H. Y. Chen, Phys. Chem. Chem. Phys. **4**, 3794 (2002).
[7]N. Guillou, L. C. Nistor, H. Fuess, and H. Hahn, Nanostruct. Mater. **8**, 545 (1997).
[8]M. Hirano and M. Inagaki, J. Mater. Chem. **10**, 473 (2000).
[9]F. Bondioli, A. B. Corradi, C. Leonelli, and T. Manfredini, Mater. Res. Bull. **34**, 2159 (1999).
[10]A. Mukherjee, D. Harrison, and E. J. Podlaha, Electrochem. Solid State Lett. **4**, D5 (2001).
[11]S. Dikmen, P. Shuk, M. Greenblatt, and H. Gocmez, Solid State Sci. **4**, 585 (2002).
[12]S. W. Zha, C. R. Xia, and G. Y. Meng, J. Power Sources **115**, 44 (2003).
[13]J. G. Li, T. Ikegami, Y. R. Wang, and T. Mori, J. Am. Ceram. Soc. **86**, 915 (2003).
[14]Y. R. Wang, T. Mori, J. G. Li, and T. Ikegami, J. Am. Ceram. Soc. **85**, 3105 (2002).
[15]B. Djuričić and S. Pickering, J. Eur. Ceram. Soc. **19**, 1925 (1999).
[16]M. J. Godinho, R. F. Goncalves, L. P. S. Santos, J. A. Varela, E. Longo, and E. R. Leite, Mater. Lett. **61**, 1904 (2007).
[17]R. A. Rocha and E. N. S. Muccillo, Mater. Sci. Forum **416–418**, 711 (2003).
[18]S. Wang and K. Maeda, J. Am. Ceram. Soc. **85**, 1750 (2002).
[19]H. Z. Song, H. B. Wang, S. W. Zha, D. K. Peng, and G. Y. Meng, Solid State Ionics **156**, 249 (2003).
[20]C. S. Riccardi, R. C. Lima, M. L. dos Santos, P. R. Bueno, J. A. Varela, and E. Longo, Solid State Ionics **180**, 288 (2009).
[21]R. I. Walton, Progr. Cryst. Growth Charact. Mater. **57**, 93 (2011).
[22]H. Wang, H. Nakamura, M. Uehara, Y. Yamaguchi, M. Miyazaki, and H. Maeda, Adv. Funct. Mater. **15**, 603 (2005).
[23]J. R. Dethlefsen and A. Dossing, Nano Lett. **11**, 1964 (2011).
[24]B. O. Dabbousi, J. RodriguezViejo, F. V. Mikulec, J. R. Heine, H. Mattoussi, R. Ober, K. F. Jensen, and M. G. Bawendi, J. Phys. Chem. B **101**, 9463 (1997).
[25]M. A. Hines and P. Guyot-Sionnest, J. Phys. Chem. **100**, 468 (1996).
[26]A. R. Kortan, R. Hull, R. L. Opila, M. G. Bawendi, M. L. Steigerwald, P. J. Carroll, and L. E. Brus, J. Am. Chem. Soc. **112**, 1327 (1990).
[27]L. Qi, J. Ma, H. Cheng, and Z. Zhao, Colloids Surf. A: Physicochem. Eng. Asp. **111**, 195 (1996).
[28]Z. A. Peng and X. G. Peng, J. Am. Chem Soc. **123**, 183 (2001).
[29]H. G. Zhu, A. Prakash, D. N. Benoit, C. J. Jones, and V. L. Colvin, Nanotechnology **21**(25), 255604 (2010).
[30]N. Zhang, S. Q. Liu, X. Z. Fu, and Y. J. Xu, J. Phys. Chem. C **115**, 9136 (2011).
[31]W. F. Yao and J. H. Ye, J. Phys. Chem. B **110**, 11188 (2006).
[32]Y. H. Zhang, N. Zhang, Z. R. Tang, and Y. J. Xu, Acs Nano **6**, 9777 (2012).
[33]Z. S. Pillai and P. V. Kamat, J. Phys. Chem. B **108**, 945 (2004).
[34]C. C. Chen, Q. Wang, P. X. Lei, W. J. Song, W. H. Ma, and J. C. Zhao, Environ. Sci. Technol. **40**, 3965 (2006).
[35]S. Q. Liu, N. Zhang, Z. R. Tang, and Y. J. Xu, ACS Appl. Mater. Interfaces **4**, 6378 (2012).
[36]C. T. Lee, W. T. Yang, and R. G. Parr, Phys. Rev. B **37**, 785 (1988).
[37]R. Dovesi, R. Orlando, B. Civalleri, C. Roetti, V. R. Saunders, and C. M. Zicovich-Wilson, Zeit. Kristall. **220**, 571 (2005).
[38]V. R. S. R. Dovesi, C. Roetti, R. Orlando, C. M. Zicovich-Wilson, F. Pascale, B. Civalleri, K. Doll, N. M. Harrison, I. J. Bush, P. Darco, and M. Llunell, *CRYSTAL09 User's Manual* (University of Torino, Torino, 2009).
[39]M. L. G. Anderson Reis Albuquerque, I. M. G. Santos, V. M. Longo, E. Longo, and J. Ricardo Sambrano, J. Phys. Chem. A **116**, 11731 (2012).
[40]Y. V. B. de Santana, C. W. Raubach, M. M. Ferrer, F. La Porta, J. R. Sambrano, V. M. Longo, E. R. Leite, and E. Longo, J. Appl. Phys. **110**, 123507 (2011).
[41]C. W. Raubach, Y. V. B. de Santana, M. M. Ferrer, V. M. Longo, J. A. Varela, W. Avansi, P. G. C. Buzolin, J. R. Sambrano, and E. Longo, Chem. Phys. Lett. **536**, 96 (2012).
[42]A. Beltran, J. R. Sambrano, M. Calatayud, F. R. Sensato, and J. Andres, Surf. Sci. **490**, 116 (2001).
[43]M. Mogensen, N. M. Sammes, and G. A. Tompsett, Solid State Ionics **129**, 63 (2000).
[44]X. S. Fang, T. Y. Zhai, U. K. Gautam, L. Li, L. M. Wu, B. Yoshio, and D. Golberg, Progr. Mater. Sci. **56**, 175 (2011).
[45]L. Valenzano, F. J. Torres, D. Klaus, F. Pascale, C. M. Zicovich-Wilson, and R. Dovesi, Zeit. Physik. Chem.-Int. J. Res. Phys. Chem. Chem. Phys. **220**, 893 (2006).
[46]M. Dolg, H. Stoll, and H. Preuss, J. Chem. Phys. **90**, 1730 (1989).
[47]T. Desaunay, A. Ringuede, M. Cassir, F. Labat, and C. Adamo, Surf. Sci. **606**, 305 (2012).
[48]J. Jaffe and N. W. Ashcroft, Phys. Rev. B **27**, 5852 (1983).
[49]A. Lichanot, E. Apra, and R. Dovesi, Phys. Status Solidi B-Basic Res. **177**, 157 (1993).
[50]A. Kokalj, Comput. Mater. Sci. **28**, 155 (2003).
[51]See supplementary material at http://dx.doi.org/10.1063/1.4880795 for XRD peaks width (FWHM) of the samples; Theoretical and experimental lattice parameters (in Å) for CeO_2 and ZnS; FT-IR spectra in the 400 to 4000 cm^{-1} of the CeO_2, ZnS and CeO_2@ZnS nanoparticles (a) in EG (b) H_2O; band structure of (a) CeO_2–o and (b) CeO_2–d; and band structure of (a) ZnS–o and (b) ZnS–d.
[52]D. Chen, F. Huang, G. Ren, D. Li, M. Zheng, Y. Wang, and Z. Lin, Nanoscale **2**, 2062 (2010).
[53]G. Q. Ren, Z. Lin, B. Gilbert, J. Zhang, F. Huang, and J. K. Liang, Chem. Mater. **20**, 2438 (2008).
[54]R. M. Salavati, M. Niasari, and D. Ghanbari, J. Nanostruct. **1**, 231 (2012).
[55]Y. Y. She, J. Yang, and K. Q. Qiu, Trans. Nonferrous Met. Soc. China **20**, S211 (2010).
[56]J. F. Xu, W. Ji, J. Y. Lin, S. H. Tang, and Y. W. Du, Appl. Phys. A-Mater. Sci. Process. **66**, 639 (1998).
[57]C. Binet, M. Daturi, and J. C. Lavalley, Catal. Today **50**, 207 (1999).
[58]X. Du, L. Dong, C. Li, Y. Liang, and Y. Chen, Langmuir **15**, 1693 (1999).
[59]N. C. Wu, E.-W. Shi, Y.-Q. Zheng, and W.-J. Li, J. Am. Ceram. Soc. **85**, 2462 (2002).
[60]V. Venkataramanan, H. L. Bhat, M. R. Srinivasan, P. Ayyub, and M. S. Multani, J. Raman Spectrosc. **28**, 779 (1997).
[61]P. Biddle and J. H. Miles, J. Inorg. Nucl. Chem. **30**, 1291 (1968).
[62]V. Venkataramanan, M. R. Srinivasan, and H. L. Bhat, J. Raman Spectrosc. **25**, 805 (1994).
[63]K. Nakamoto, *Infrared Spectra of Inorganic and Coordination Compounds* (John Wiley & Sons, Inc., London, 1963).
[64]M. Kieninger and O. N. Ventura, Int. J. Quant. Chem. **111**, 1843 (2011).
[65]C. Sun, H. Li, and L. Chen, J. Phys. Chem. Solids **68**, 1785 (2007).
[66]C. Sun, J. Sun, G. Xiao, H. Zhang, X. Qiu, H. Li, and L. Chen, J. Phys. Chem. B **110**, 13445 (2006).
[67]R. Yu, L. Yan, P. Zheng, J. Chen, and X. Xing, J. Phys. Chem. C **112**, 19896 (2008).
[68]J. McBride, J. Treadway, L. C. Feldman, S. J. Pennycook, and S. J. Rosenthal, Nano Lett. **6**, 1496 (2006).
[69]S. J. Rosenthal, J. McBride, S. J. Pennycook, and L. C. Feldman, Surf. Sci. Rep. **62**, 111 (2007).
[70]J. Tauc, Mater. Res. Bull. **3**, 37 (1968).
[71]M. Cardona and G. Harbeke, Phys. Rev. **137**, A1467 (1965).
[72]T. K. Tran, W. Park, W. Tong, M. M. Kyi, B. K. Wagner, and C. J. Summers, J. Appl. Phys. **81**, 2803 (1997).
[73]W. Chen, Z. G. Wang, Z. J. Lin, and L. Y. Lin, Appl. Phys. Lett. **70**, 1465 (1997).
[74]R. M. Bueno, J. M. Martinez-Duart, M. Hernandez-Velez, and L. Vazquez, J. Mater. Sci. **32**, 1861 (1997).
[75]T. Masui, K. Fujiwara, K.-i. Machida, G.-y. Adachi, T. Sakata, and H. Mori, Chem. Mater. **9**, 2197 (1997).
[76]M. Inoue, M. Kimura, and T. Inui, Chem. Commun. **1999**(11), 957–958.
[77]J. Graciani, A. M. Marquez, J. J. Plata, Y. Ortega, N. C. Hernandez, A. Meyer, C. M. Zicovich-Wilson, and J. F. Sanz, J. Chem. Theory Comput **7**, 56 (2011).
[78]C. W. Raubach, M. Z. Krolow, M. F. Mesko, S. Cava, M. L. Moreira, E. Longo, and N. L. V. Carreno, Crystengcomm **14**, 393 (2012).
[79]F. A. La Porta, M. M. Ferrer, Y. V. B. de Santana, C. W. Raubach, V. M. Longo, J. R. Sambrano, E. Longo, J. Andrés, M. S. Li, and J. A. Varela, J. Alloys Compd. **556**, 153 (2013).
[80]H.-L. Fei, H.-J. Zhou, J.-G. Wang, P.-C. Sun, D.-T. Ding, and T.-H. Chen, Solid State Sciences **10**, 1276 (2008).
[81]A. Franco, M. C. Neves, M. M. L. R. Carrott, M. H. Mendonça, M. I. Pereira, and O. C. Monteiro, J. Hazard. Mater. **161**, 545 (2009).